Self-Assembled Dichroic Plasmonic Nitride Nanostructures with Broken Centrosymmetry

Journal:	*ACS Nano*
Manuscript ID	Draft
Manuscript Type:	Article
Date Submitted by the Author:	n/a
Complete List of Authors:	Babonneau, David; Université de Poitiers, Métallurgie Physique Camelio, Sophie; Université de Poitiers, Institut Pprime ABADIAS, Gregory; Universite de Poitiers, Institut Pprime Christofilos, Dimitris; Aristotle University of Thessaloniki, School of Chemical Engineering Arvanitidis, Ioannis; Aristotle University of Thessaloniki, Physics Psilodimitrakopoulos, Sotirios; Foundation of Research and Technology Hellas, Institute of Electronic Structure and Laser Maragkakis, George; Foundation of Research and Technology Hellas, Institute of Electronic Structure and Laser Stratakis, Emmanuel; Institute of Electronic Structure and Laser, Kalfagiannis, Nikolaos; Nottingham Trent University, School of Science and Technology ΠΑΤΣΑΛΑΣ, ΠΑΝΑΓΙΩΤΗΣ; Aristotle University of Thessaloniki, Physics

SCHOLARONE™
Manuscripts

Self-Assembled Dichroic Plasmonic Nitride Nanostructures with Broken Centrosymmetry

D. Babonneau[1], S. Camelio[1], G. Abadias[1], D. Christofilos[2], J. Arvanitidis[3], S. Psilodimitrakopoulos[4], G.M. Maragkakis[4], E. Stratakis[4], N. Kalfagiannis[5], P. Patsalas[1,3,]*

[1]Institut Pprime, UPR 3346 CNRS-Université de Poitiers-ENSMA, Département Physique et Mécanique des Matériaux, 86073 Poitiers, France

[2]Aristotle University of Thessaloniki, Faculty of Engineering, School of Chemical Engineering and Physics Laboratory, 54124 Thessaloniki, Greece

[3]Aristotle University of Thessaloniki, Department of Physics, 54124 Thessaloniki, Greece

[4]Institute of Electronic Structure and Laser, Foundation for Research and Technology-Hellas, Heraklion Crete, 71110, Greece

[5]School of Science and Technology, Nottingham Trent University, Nottingham, NG11 8NS, United Kingdom

*Corresponding author: ppats@physics.auth.gr

KEYWORDS

Refractory conductors; Plasmonics; Bottom-Up Fabrication; Defects; Second Harmonic Generation

1

ABSTRACT

TiN and ZrN are emerging as important alternative plasmonic materials. In addition to their well-known assets, they can incorporate point defects that break the centrosymmetry of their cubic crystal structure, making them promising candidates as non-linear optical materials and especially for second harmonic generation (SHG). Their refractory character and chemical stability were obstacles for the bottom-up fabrication of TiN and ZrN nanostructures so far. In this work, it is shown that highly directional dichroic nanostructures of TiN and ZrN may be indeed grown by self-assembly using glancing angle deposition on periodic rippled dielectric surfaces. The produced nitride nanostructures exhibit point defects and exceptional photothermal durability. These nanostructures exhibit strong SHG response when probed by a near-infrared laser. It is shown that SHG is strongly associated with the near-field enhancement due to the localized surface plasmon resonance of the nanostructures. Given that such nanostructures can endure extremely high electric fields, they are expected to be able to emit massive SHG signals.

I. INTRODUCTION

Transition metal nitrides (TMNs), predominantly TiN and ZrN, are well-known optical conductors. Concomitantly, surface plasmon polaritons at TiN surfaces and localized surface plasmon resonance (LSPR) at TiN nanoparticles were observed as early as 2004 by Patsalas *et al.* [1] and Reinholdt *et al.* [2], respectively. In 2011, TMNs were proposed for the first time as realistic alternative materials for plasmonic devices by Naik *et al.* [3] due to the extraordinary combination of their properties that include refractory

character [4], chemical and mechanical stability [5-8], and durability to high electric

fields [9]; the latter also opens substantial opportunities for non-linear optics [9-11].

Since then, the relevant scientific interest, as attested by the number of published papers,

shows a geometrical growth with an annual increase over 60%. However, most of these

works do not report the realization of TMN nanostructures in microelectronic

architectures, instead they are dealing with continuous TMN layers (*e.g.* Ref. 12-16),

computational works (*e.g.* Ref. 17-21), works evaluating the plasmonic potential of

certain continuous films via their dielectric permittivity (*e.g.* Ref. 4, 20-24) and

implementing specific figures of merit [25, 26], or colloidal nanoparticles [27-29] and

powders [30, 31]. This is mostly due to the difficulty of the bottom-up fabrication of

nitride nanostructures due to their refractory character and to the covalent metal-nitrogen

bonding [32] that prevent the melting and resolidification in realistic temperatures, as

well as the differing optical properties of ultrathin TiN films compared to their opaque

counterparts [1, 33]. As a result, only a few experimental works can be found reporting

the top-down fabrication of plasmonic devices [34-41]. In particular, the patterning

methods employed so far for the fabrication of TiN and ZrN nanostructures include direct

focused ion beam patterning [34], the combination of electron beam lithography [35-38]

or nanoimprint lithography [39, 40] with reactive ion etching, and laser interferometry

patterning with wet chemical etching [9, 41].

The quality of TMN films can vary significantly depending on the particular

choice of one of the many available growth techniques. There is, unfortunately, a feature

that is present in all manufacturing schemes: TMNs typically contain a considerable

amount of point defects that are known to affect the properties of the host crystal [42, 43].

Such difficulty in producing defect-free, ultra-thin TMNs, due to their refractory

character, may turn from a curse into a blessing in the field of non-linear optics. The

included point defects break locally the centrosymmety of the cubic structure, as attested

by the Raman spectra of TMNs [44, 45]; the symmetry breaking is an essential

prerequisite for the manifestation of second harmonic generation (SHG) [46, 47].

In this work, a large-scale, bottom-up, maskless, and etchless fabrication process

of strongly dichroic and plasmonic TiN and ZrN nanostructures is presented. It is based

on glancing angle deposition (GLAD) [48, 49] and reactive magnetron sputtering on

prepatterned substrates [50]. The produced TiN and ZrN nanostructures have the form of

aligned nanowires (NWs) with a more-or-less granular morphology, and they exhibit

strong dichroism in the visible and near-infrared (NIR) ranges, as well as exceptional

photothermal durability. The coherency of the nanostructures may be compromised in the

case of multi-stack deposition that results in strong scattering of light. Thus, strong SHG

may be present in such systems. Its occurrence is closely coupled with the plasmon

resonance while its directionality is associated with the coherence of the nanostructures.

II.   RESULTS AND DISCUSSION

a.   *Fabrication Concept and Morphology of Nanostructures*

The steps of the reported self-assembly process are summarized in Fig. 1a. The

selection of substrate is not critical as long as it is atomically flat. In this work, two

substrates were implemented: fused silica for optical transmission measurements and

SHG experiments, and conductive *n*-type Si(100) wafers (covered with a 2-nm thick native oxide layer) for Raman spectroscopy experiments, as well as for morphology characterizations via Atomic Force Microscopy (AFM) measurements.

Amorphous alumina layers, 170 nm thick, were deposited on top of the various substrates by dual ion beam sputtering (DIBS) as described in more detail in Ref. 50. The second step of the process is the patterning of the amorphous alumina thin film by 1 keV-Xe^+ ion bombardment at oblique incidence (55°) to form periodic nanoripples [50]. The third step is the GLAD of TiN and ZrN on the rippled alumina surface via reactive magnetron sputtering. This step is particularly challenging for TiN and ZrN due to the combination of the reactive process associated with GLAD geometry, the high melting points of TiN and ZrN [21], the cohesive energies of Ti and Zr [51], the low work function [52], and the ionization potential [53] of TiN and ZrN compared to Ag and Au. As a result, the TiN and ZrN reactive sputtering growth lies into the Zone 1 of limited diffusion and of high density of structural defects, according to the updated structural zone model of Anders [54], in contrast to Au and Ag that lie in Zone 3 of high crystallinity due to diffusion of adatoms [54]. In order to overcome these obstacles, the GLAD deposition (5° angle of incidence) of TiN and ZrN was performed by reactive magnetron sputtering in the metallic cathode mode (*i.e.* strictly preventing poisoning of the target). The reactive gas (N_2) flow was delivered exclusively close to the substrate by a dedicated gas line monitored by a real-time mass spectrometer, and the ion bombardment conditions were kept mild and below the subplantation threshold [55] by applying a bias of -60 V to the substrate during growth. The substrate temperature was tuned to 500 °C, in order to maximize the surface diffusion of the deposited adatoms [54,

5

55], while preventing the oxidation of the deposited nanostructures via diffusion of oxygen from the underlying alumina into the nitride (a process that might occur at 600 ^{o}C [7]). The deposition conditions used for this step are summarized in Table 1. The geometry of this step enables the growth of self-assembled and well-aligned nanostructures along the ripples, as we will show below, all over a macroscopic area, which is comparable to USD and Euro coins (shown in Fig. 1b).

Then, a selection of samples proceeded to step 4, which is the *in situ* capping by an ultra-thin (5 nm) amorphous SiN_x layer, grown by RF magnetron sputtering from a Si_3N_4 ceramic target, in order to prevent oxidation and provide long-term stability to the nanostructures [30]. SiN_x was selected due to its dielectric character as well as the thermal stability of the conductive nitride/Si_3N_4 nanostructures [56]. For selected samples, steps 3 and 4 were repeated *in situ* to form multi-stacks of TiN or ZrN nanostructures to enhance their far-field plasmonic features.

The formation of periodic ripple patterns on amorphous alumina surfaces subjected to 1 keV-Xe^+ ion bombardment at oblique incidence is well-documented and robustly reproducible [48-50]. The process results in near-parallel and slightly wavy ripples perpendicular to the ion-beam projection, as shown in the AFM images in the upper side of Fig. 2, all over the area of a macroscopic sample as shown in Fig. 1b. The AFM images can be quantified by considering the height variations along line scans in directions parallel or perpendicular to the ripples, as shown in Fig. S1 of on-line supplemental information. The height variations along the bare ripples are negligible, while the height variations across the ripples indicate a period Λ of 26.0±1.1 nm, and an

6

average peak-to-valley height of 2.6±0.2 nm (note that the reported height and period

values might be slightly affected by the radius of curvature of the tip, which is ~10 nm).

After the GLAD of TiN at 500 ºC (Fig. 2, intermediate panels, and Fig. S1, green

lines), the ripples retain their morphology and only some faint grainy structures appear at

the highest resolution, which indicate the formation of continuous, yet rough, TiN NWs

along the ripples. The difference of the determined period of the ripples after TiN

deposition (Λ = 28.6±1.5 nm) from the bare ripples is within the experimental error,

while the peak-to-valley height across the ripples increases after TiN deposition to

3.3±0.4 nm. Along the ripples, the root mean square roughness increases after TiN

deposition, but no individual TiN nanoparticles can be identified.

The GLAD of ZrN results in a quite different morphology (Fig. 2, lower panels,

and Fig. S1, magenta/purple lines). Again, the period of the nanostructures across the

ripples (Λ = 29.6±2.2 nm) is not substantially different from that of the bare ripples.

However, the average peak-to-valley height becomes 4.5±0.7 nm, indicating significant

growth of ZrN on the alumina ripples. More striking differences are observed along the

ripples after ZrN deposition. Indeed, clear features, characteristic of granular ZrN

nanostructures, are identified along the ripples; their period and average peak-to-valley

height are 19.1±3.4 nm and 1.5±0.1 nm, respectively. Based on the observed

morphologies and the quantitative data, it can be safely concluded that ZrN after GLAD

forms highly oriented arrays of densely-packed nanoparticles resulting in granular-like

NWs along the underlying ripples. The difference in the morphology of the produced TiN

and ZrN nanostructures, *i.e.* quite smooth NWs *vs* arrays of granular NWs, respectively,

may be assigned to a variety of reasons, such as differences in angular and energy

distribution of sputtered atoms reaching the substrate at glancing angle, and the reduced

mobility of Zr adatoms on the active growing surface [57, 58]. The reported

morphological features do not change after the deposition of the homogeneous 5 nm

ultrathin SiN_x capping layer over the TiN or ZrN nanostructures (Fig. 1a, step 4). When

the GLAD of TiN or ZrN and the sputter deposition of the homogenous SiN_x capping

layer are repeated three times, in order to produce triple arrays of nanostructures and

increase their linear as well as non-linear plasmonic response, the surface morphology of

the top array of nanostructures is less organized and coherent as it is shown in the on-line

supplemental information (Fig. S2). A possible explanation for this difference in

morphology is most likely due to the roughness and morphology of the underlying layers

of nanostructures that alter the shadowing and surface diffusion conditions during GLAD.

Such loss of coherency sets the limit of repetitions in this process and defines the

maximum interaction volume with the incident light; it also affects the linear and non-

linear optical properties of the TMN nanostructures, as it will be discussed later.

It is worth noting that the proposed process is generic and might be very efficient

for the production of nanostructures of a wide variety of alternative non-metallic

conductors, which are usually grown by sputter deposition, such as molybdenum nitride

(MoN) [59], tantalum nitride (TaN) [20, 22 60], niobium nitride (NbN) [61], In-doped tin

oxide (ITO) [22, 62, 63], aluminum- or gallium-doped zinc oxide (AZO, GZO) [22, 62,

64, 65], niobium-doped titanium oxide (NTO) [66], partly reduced molybdenum oxides

MoO_x (x<3) [67, 68], and vanadium dioxide (VO_2), which exhibits a metal-insulator

transition [69, 70]. All these conductors have been proposed as alternative plasmonic

materials, whose plasmonic activity spans the far ultraviolet to medium infrared range [1, 20, 22, 59, 61, 71-79].

b. *Vibrational Properties and Photothermal Stability*

In addition to the morphological features, it is important to clarify whether the formed TMN nanostructures adopt the B1 rocksalt crystal structure, which is the phase that exhibits strong plasmonic performance [21, 45], or not. The Raman spectra of ZrN and TiN are characterized by distinct features [44, 45, 80-84], which are associated with the first order transverse acoustic (TA) and longitudinal acoustic (LA) modes. These peaks are normally forbidden because of the O_h symmetry of the rocksalt structure, and they emerge only in the presence of defects that break the local symmetry. Therefore, the usefulness of the Raman spectra is twofold; it serves the non-destructive identification of the B1 rocksalt phases of ZrN and TiN, as well as the detection of point defects that break the symmetry of the cubic, centrosymmetric ZrN and TiN.

Figure 3 shows the polarized Raman spectra of the ZrN and TiN nanostructures (both single- and triple-arrays) with the electric field of the probe laser beam being linearly polarized across (denoted $\perp$ for perpendicular) or along (denoted $\parallel$ for parallel) the ripples. For the Raman experiments, silicon replaced silica as the substrate for the process presented in Fig. 1, in order to eliminate the broad Raman signal from silica [73] that overlaps with the spectra of TiN and ZrN. The corresponding Raman spectra from opaque epitaxial films from Ref. 81 are also shown for comparison. All the spectra exhibit a doublet at low frequencies (below 350 cm^{-1}), which is assigned to the first order TA and LA modes. As mentioned previously, this doublet is exclusively due to the

presence of point defects that break the O_h symmetry of the rocksalt (B1) structure. The Raman features at higher frequencies originate from the overlapping of the first order optical (O) and the second order acoustic modes (2A), according to Spengler *et al.* [44]. The comparison of the Raman spectra of the nanostructures with those of the epitaxial films firmly identifies the B1 rocksalt crystal structure. This was further confirmed by X-ray and electron diffraction studies (not reported here). The epitaxial films exhibit sharper features than the reported nanostructures due to the improved crystallinity. It is important to note that for all samples, there is no significant change of the broadening of the Raman features between the spectra of the two beam polarizations (along and across the ripples), indicating that there is no preferable axis of improved crystallinity despite of the linear ordering of the nanostructures along the ripples.

Spengler *et al.* also associated the intensity ratio of the first order acoustic modes and the broad envelope of O and 2A modes with the density of point defects that break locally the O_h symmetry. Indeed, it has been very recently demonstrated that this ratio is well-scaled with the formation energy of vacancies in all the conductive TMNs [81]. The frequencies ω_{TA}, ω_{LA}, $\omega_{O\&2A}$ of the TA, LA modes and of the O&2A envelope, respectively, as well as the intensity ratio $I_{TA}/I_{O\&2A}$ of the TA peak over the O&2A envelope are summarized in Tables S1 and S2 of the on-line supplemental information for ZrN and TiN, respectively. Several aspects have been revealed from the quantitative results. Firstly, the frequencies of the TA and LA modes and the O&2A envelope of the epitaxial films are in remarkable agreement with previous studies on stoichiometric nitrides [44, 82, 83]. Secondly, the TA and LA modes of both TiN and ZrN nanostructures are shifted compared to the corresponding epitaxial films; this is more

pronounced for the TA mode that exhibits shifts higher than 17 cm^{-1} and 5 cm^{-1} for TiN

and ZrN, respectively. Such shifts were assigned to deviations from stoichiometry both

for TiN [44, 83] and ZrN [84]. Therefore, the produced TMN nanostructures may not be

stoichiometric. Importantly, for the SHG applications, the $I_{TA}/I_{O\&2A}$ ratio is increased by

66% and 18% in TiN and ZrN nanostructures, respectively, compared to the epitaxial

samples. This ratio was associated with the point defects [81] and the results show that

the TiN nanostructures incorporate more defects than the ZrN nanostructures. Indeed, it

was shown that at the very initial stages of growth, for thickness less than 6 nm, TiN is

not stoichiometric and exhibits a high concentration of defects [1]. Last but not least, this

ratio does not vary significantly along and across the ripples indicating that there is no

preferred directionality for the accumulation of defects.

The Raman experiments may also be used to test the photothermal stability of the

produced nanostructures. To check and demonstrate the photothermal stability, especially

across the ripples where the size of the nanostructures is just few nanometers, Raman

spectra were acquired from the single-array ZrN nanostructures with polarization across

the ripples, varying the power of the probe laser beam. The relevant spectra for 1, 5, and

20 mW continuous wave laser probe are shown in the upper panel of Fig. 3 with different

shades of grey; all the spectra are identical with no traces of oxidation or formation of

additional defects in the ZrN nanostructures. Given that the spot size of the probe laser

beam is ~1 μm on sample, the maximum power density used is 2.5 MW/cm^2, which is

one order of magnitude higher than the power density used for the sintering of colloidal

Ag inks [85] and comparable with the pulsed laser power used for the melting of Ag

layers [86] and the diffusion of melted Ag out of yttria scaffolds [87]. Therefore, the ZrN

nanostructures exhibit remarkable and extraordinary photothermal stability that easily outperforms plasmonic Ag nanostructures.

c. *Linear and Non-Linear Optical Properties*

The far-field optical properties of the formed TMN nanostructures are characterized by strong dichroism and plasmonic effects. This is clearly demonstrated in the polarized optical absorbance spectra of Fig. 4 (calculated from raw optical transmission spectra). The left and center panels show the optical absorbance spectra for two bare and two SiN_x-capped TiN and ZrN arrays of nanostructures, respectively, with electric field across ($\perp$, solid lines) and along ($\parallel$, dotted lines) the ripples. For both cases, the dichroism is not prominent for short wavelengths (shorter than 400 nm or 3.1 eV and 350 nm or 3.5 eV for TiN and ZrN, respectively); the increased absorbance in this range is due to the interband transitions of TiN and ZrN and it is consistent with the interband absorption reported for continuous opaque TiN and ZrN films [1, 20, 21, 45].

In the case of the bare TiN nanostructures, there is a strong dichroism mostly in the NIR range, with a prominent localized absorbance peak centered around 1200 nm (1.03 eV) for the electric field in the perpendicular direction, *i.e.* across the ripples and nanostructures. This peak is assigned to LSPR due to the infinitesimal size of the TiN nanostructures across the alumina ripples. The plasmonic hypothesis is confirmed by the comparison of the optical absorbance spectra of bare (Fig. 4, red solid line) and SiN_x-capped nanostructures (Fig. 4, orange solid line). The absorbance peak of the SiN_x-capped nanostructures is substantially redshifted to 1860 nm (0.67 eV) due to the higher refractive index of the surrounding SiN_x (n~2) compared to air (n~1), as indicated by the

black arrows. This proves unequivocally the plasmonic nature of this optical feature. The

LSPR of the bare TiN nanostructures lies into the NIR range and not in the visible as it

would be anticipated for spherical nanoparticles [21]. This can be explained by the high

concentration of defects, as indicated by the Raman spectra, as well as the flatness of the

TiN NWs and the short edge-to-edge distance between NWs. LSPR can be also

substantially redshifted and weakened in ultrathin TiN due to stoichiometry variations

[88] and the incorporation of surface oxygen species [89], which are both depleting the

conduction electrons. In addition, it was previously shown that for ultra-thin TiN deposits

(<6 nm) the nitride is inherently defective even if the deposition conditions are

appropriate for the growth of stoichiometric TiN at higher thicknesses [1]. In the parallel

direction of the electric field (along the ripples and nanostructures), no such peaks are

observed in the experimental spectral window, and therefore the optical response of TiN

nanostructures is more consistent with an infinite 1D conductor.

The case of the ZrN nanostructures is more complex and interesting. The

dichroism and the plasmonic features are manifested not only in the NIR, but also extend

into the visible range (Fig. 4, center panel). In the perpendicular direction of the electric

field (across the ripples), the LSPR of bare ZrN nanostructures is vaguely manifested

through a shoulder around 500 nm (2.48 eV) (Fig. 4, blue solid line), a value consistent

with what would be expected for ZrN spherical nanoparticles [21, 45]. This LSPR is

redshifted, like in the case of TiN, to 580 nm (2.14 eV) for the SiN_x-capped ZrN

nanostructures (Fig. 4, cyan solid line). However, as opposed to the case of TiN NWs, for

the parallel field (along the ripples) both bare and SiN_x-capped ZrN nanostructures

exhibit another plasmonic absorption band in the NIR around 1130 and 1200 nm (1.10-

1.03 eV), respectively. In contrast to TiN, where dichroism originates from the existence

or not of a plasmonic absorption band, in ZrN nanostructures the dichroism is due to the

existence of two distinct plasmonic features at the two polarizations of the incident light.

While the LSPR in the visible range and for the perpendicular field is very well

understood and resembles the optical response of the TiN nanostructures, the nature of

the plasmonic feature in the NIR for the parallel field may originate from the granular

structure of the ZrN nanostructures. Indeed, the particle-particle near field interaction of

the ZrN dense granular nanostructure may result in the observed substantial redshift [90-

92]. Finally, the ZrN and TiN multi-stacks retain the plasmonic features of their capped

single-array counterparts, albeit with stronger far-field optical absorption due to the

cumulative interactions of each array of nanostructures with the incoming light (Fig. 4,

right panel).

In order to shed some light on the plasmonic performance of the ZrN and TiN

nanostructures interacting with the perpendicular electric field ($\perp$), Finite-Difference

Time-Domain (FDTD) calculations were carried out. An in-house 3D FDTD simulator

[93, 94] was used in all calculations. Arrays of one-dimensional rods with infinite length

and semi-elliptic cross section at a constant center-to-center distance of $\Lambda = 30$ nm

(roughly the period of ripples on the substrate) were considered for the calculations, as

shown in Fig. 5a. The calculations were carried out for a range of aspect ratios H/D

(where H and D are the height and diameter of the rods, respectively) in adequacy with

the AFM experimental observations and with the aim of reproducing the experimental

position of the absorbance maxima. We used dielectric functions retrieved from

ellipsometric measurements of continuous opaque ZrN and TiN films deposited at near-

normal incidence in the same conditions as the TMN nanostructures. The incoming

electric field was set perpendicular ($\perp$) to the infinite axes of the rods. The far-field

optical absorbance (see on-line supplemental information, Fig. S3), as well as the

distributions of the electric near-field enhancement (NFE) for the excitation wavelength

(1030 nm) of the laser used for the SHG experiments, were calculated. The FDTD results

unequivocally show that the far-field properties (Fig. S3) are substantially affected by the

morphology of the nanostructures, as it is shown in the contour plots of the wavelength of

the absorbance maximum for varying D and H values for ZrN (Fig. 5b) and TiN (Fig.

5c). In Fig. 5c (upper panel), the thick green line corresponds to the experimental position

of the LSPR maximum for the bare TiN nanostructures (*i.e.*, 1200 nm). Our calculations

confirm that the LSPR redshift compared to the expected position for spherical TiN

nanoparticles in air (520 nm [1]) originates from flat and coupled TiN NWs. Several

(H,D) couples lead to consistency between the experimental and calculated spectral

positions of LSPR maximum. Nevertheless, considering the nominal equivalent

thickness of TiN (3.7 nm, Table 1), the best (*H,D*) couple that could explain the

experimental position is $D = 28$ nm and $H = 2.4$ nm, corresponding to very flat (*H/D* <

0.1) and highly coupled ($x = \Lambda - D = 2$ nm $< D/10$) TiN nanostructures. The existence of

nanogaps between plasmonic nanostructures associated with LSPR coupling were

reported to result in strong redshift of the far-field absorbance and reflectance as well as

exceptional NFE at the formed hot spots [95]. As shown in Fig. 5c (lower panel), the

corresponding calculated positions of the LSPR for SiN_x-capped TiN nanostructures are

even more redshifted in the NIR in agreement with the experimental observations. In the

case of ZrN nanostructures, considering a nominal equivalent thickness of 7.6 nm (Table

1), the best (H,D) couple that explains the experimental position of LSPR maximum for

the SiN$_x$-capped sample, which is clearly identified at 580 nm in Fig. 4, center panel (see

thick green line in the contour plot of Fig. 5b, lower panel), is $H = 17$ nm and $D = 18$ nm.

Therefore, for the ZrN nanostructures, the out-of-plane aspect ratio H/D is close to 1 (0.9)

with an edge-to-edge distance $x = 12$ nm (higher than $D/2$). The corresponding calculated

position of the LSPR maximum for the bare ZrN nanostructures is obtained at 515 nm

(Fig. 5b, upper panel) in line with the experimental shoulder around 500 nm (Fig. 4,

center panel). In that case, FDTD calculations show that the deviation from what is

expected for spherical nanoparticles in air in terms of LSPR spectral position is less

prominent. The distributions of NFE at 1030 nm (the excitation wavelength which was

used for the SHG experiments) for simulated bare nanostructures with appropriate (H,D)

values are shown in Fig. 5d,e. In both cases, the maximum NFE is located at the bases

and edges of the nanostructures. The NFE in the case of 'isolated' ZrN nanostructures is

moderate (~30) and it is remarkably enhanced for the case of the coupled TiN

nanostructures (~100) due to the formation of hot spots.

By comparing the Raman with the optical absorbance spectra, we reveal an

extraordinary feature of conductive albeit defective nitride nanostructures: TMNs exhibit

a unique combination of broken centrosymmetry (due to defects and refractory character)

and plasmonic activity with great potential for SHG. This is in contrast to the traditional

plasmonic metals (Au, Ag), which exhibit zero second-order susceptibility due to their

centrosymmetric *fcc* crystal structure [96-98]. Continuous stoichiometric TiN films

exhibit very weak SHG [99], possibly due to the low concentration of defects in such TiN

structures. Although the crystal symmetry may be broken at metallic surfaces [96], for

centrosymmetric nanostructures (as those presented in this work) the contribution of two

opposing surface elements cancels out in the far-field in the dipole approximation [97,

98]. Consequently, plasmonic nanostructures consisting of Au or Ag that are capable of

SHG are based on metamaterials with non-centrosymmetric shapes [98, 100-102]. In the

same context, TiN was implemented as a conventional metal component of non-

centrosymmetric metamaterials, such as split-ring resonators [103] and chiral core-shells

[104] for SHG, regardless of its own intrinsic broken centrosymmetry. So far, there is no

report on optical non-linearities of ZrN whatsoever.

Figure 6 shows the polar diagrams of polarized SHG (PSHG) with a pump beam

of 1030 nm (1.204 eV) using the same gain for all cases; in this diagram zero degree is

for the electric field of the pump beam being aligned along the ripple direction. An

exceptionally interesting observation is that the SHG is emitted along (‖ field) the ripples

for ZrN and across (⊥ field) the ripples for TiN. This strikingly different behavior of the

two sets of TMN nanostructures may be well explained if we consider their optical

properties presented in Fig. 4. Indeed, ZrN exhibits a broad LSPR band around 1200 nm

(1.03 eV) when the electric field of the light is parallel to the ripples, while TiN exhibits a

similar LSPR band around 1200 nm (1.03 eV) when the electric field is perpendicular to

the ripples; in both cases the 1030 nm probe beam lies within the bandwidth of the LSPR,

while it lies far beyond the strong LSPR of ZrN across the ripples (< 600 nm). So, the

TMN nanostructures act simultaneously as the probe (defects and broken

centrosymmetry) and pump (LSPR field enhancement) medium for SHG. Note that this

plasmon-pumped generation of second harmonic is contrastingly different to the work of

Huang *et al* [105], where the SHG from the defective tantalum nitride (TaN) is pumped

by the enhanced near field due to the LSPR in adjacent gold nanopillars, *i.e.* the pumping plasmon is not due to the nitride conductor itself.

The SHG is apparently stronger for ZrN, although TiN seems more defective both in the Raman (Fig. 3) and absorbance (Fig. 4) spectra. This might be attributed to the stronger LSPR in NIR for ZrN nanostructures, as well as the better overlap of ZrN LSPR with the probe beam. For optimal plasmon-pumped SHG in such defective TMN nanostructures there is a sensitive interplay between two competing mechanisms; a lot of defects increase the density of sites of broken symmetry, potentially enhancing the SHG, but at the same time they deteriorate the LSPR and the near-field enhancement, which is necessary for the SHG. In addition, the granular nature of the ZrN nanostructures may promote the creation of a high linear density of hot spots with great NFE along the ripples; this is supported by the redshifted LSPR along the ripples.

It is also interesting to follow the variations of directionality of PSHG polar diagrams; this is better illustrated in the cartesian SHG diagram presented in the on-line supplemental information (Fig. S4). The bare nanostructures, both ZrN and TiN, produce highly directional PSHG polar diagrams. This is well understood by considering that the non-linear dipoles, which define the directionality of SHG [106], are strictly directional due to the geometry of the pumping LSPR. The SiN_x-capping does not alter substantially the directionality. Finally, the multi-stacks clearly exhibit a partial loss of directionality, possibly due to the scattering of the SHG from the incoherent top arrays of nanostructures (see Fig. S2). Such variations of directionality along or across the ripples, or their reduction due to loss of coherence of the nanostructures, provide exceptional versatility for optical devices and applications.

18

III. CONCLUSIONS

An etchless, cost-effective and novel bottom-up fabrication route to produce nanostructures of the refractory and alternative plasmonic materials TiN and ZrN was presented. It is based on glancing angle deposition by reactive magnetron sputtering on prepatterned (nanorippled) alumina substrates. The process is generic and could be applied to a wide range of alternative plasmonic materials that are traditionally grown by reactive magnetron sputtering, such as the entirety of TMNs and transparent conductive oxides.

The produced nanostructures are nearly one dimensional, and they are strongly dichroic due to the different LSPR features along or across their axis. TiN and ZrN are refractory and so the produced nanostructures exhibit exceptional photothermal stability as demonstrated by Raman spectroscopy. Raman spectra also revealed the existence of a higher density of point defects than that of the corresponding continuous epitaxial films. Remarkably, these defects break the centrosymmetry of the cubic crystal structure of TiN and ZrN, while the plasmonic performance of the nitrides is retained. The combination of broken centrosymmetry with the plasmonic activity results in strong SHG. The directionality of the SHG depends on the type of plasmonic interaction (along the nanostructures for ZrN and across the nanostructures for TiN) and the coherence of the individual linear nanostructures.

IV. METHODS

Experiments:

The surface morphology of the nanostructures was analyzed immediately after deposition by AFM using a multimode Digital Instrument microscope operating in tapping mode at ambient conditions.

Raman spectroscopy measurements were conducted with a Horiba LabRAM HR instrument with a 515 nm excitation laser; the excitation laser was selected such that its energy is spectrally located beyond the reflectivity edge of TiN and ZrN and, therefore, to minimize the skin effect. A linearly polarized excitation beam was used to identify potential variations of the Raman spectra with beam polarization parallel ($\parallel$) or perpendicular ($\perp$) to the TiN and ZrN nanostructures.

The far-field optical response of the self-assembled nanostructures was investigated by means of transmission spectroscopy using a Cary 5000 spectrophotometer from Agilent Technologies equipped with a rotating polarizer. Transmittance measurements were performed at normal incidence (beam diameter $\sim$3 mm) in the spectral range 250-2200 nm (4.96-0.56 eV) with a 1 nm step using parallel ($\parallel$) or perpendicular ($\perp$) polarization with respect to the alumina ripple direction.

Polarization-resolved SHG measurements were carried out using a custom-built laser scanning microscope as described in detail in Ref. 47, using the beam from a diode-pumped Yb:KGW fs oscillator (1.2 W, 1030nm, 70–90 fs, 76 MHz, Pharos-SP, Light Conversion) and an inverted microscope (Axio Observer Z1, Carl Zeiss).

Computational Method:

The calculations of the optical response of the TiN and ZrN nanostructures were performed by time-integrating Maxwell's equations on a computational grid utilizing the Finite-Difference Time-Domain (FDTD) method, using an in-house built 3D simulator provided by E. Lidorikis [93, 94]; key features of the results were confirmed by FDTD calculations using Lumerical™.

In the computational process, the material dispersion is introduced in the form of polarization equations coupled and solved concurrently with Maxwell's equations. To accurately reproduce the optical constants of B1-TiN and B1-ZrN, within the FDTD framework, we performed a Drude-Lorentz fit [21, 45] to the experimental dielectric functions of opaque stoichiometric ZrN and TiN films obtained in the same conditions and measured by spectroscopic ellipsometry.

Table 1: Conditions of the GLAD growth of TiN and ZrN

	TiN	ZrN
DC Cathode Power (W)	300	300
Angle of Incidence (^{o})	5	5
N_2 flow at the substrate (sccm)	0.3	0.5
Ar flow at the cathode (sccm)	12	15
Partial pressure of N_2 (mbar $\times 10^{-5}$)	5-7	5-7
Working pressure (mbar $\times 10^{-3}$)	2.3	2.6
Base Pressure (mbar $\times 10^{-8}$)	<5	<5
Substrate Temperature (^oC)	500	500
DC Negative Bias Voltage (V)	60	60
Deposition Time (s)	80	120 single 80 multi[*]
Nominal equivalent thickness (nm)	3.7	7.6

*The deposition time used for ZrN multistacks was shorter than that for single arrays of nanostructures in order to minimize the loss of organization of the upper layer due to the granular morphology of the underlayers.

(a)

Step 1: Template Formation
Deposition of Alumina on a flat substrate

Step 2: Ripple Formation
1 keV Xe⁺ ion bombardment at oblique incidence (55°)

Step 3: Nanowire Deposition
Reactive sputtering of TiN or ZrN at Glancing Angle (5°) Deposition (GLAD) conditions

Step 4: Capping
RF sputtering of SiN_x at Near-normal Deposition conditions

(b)
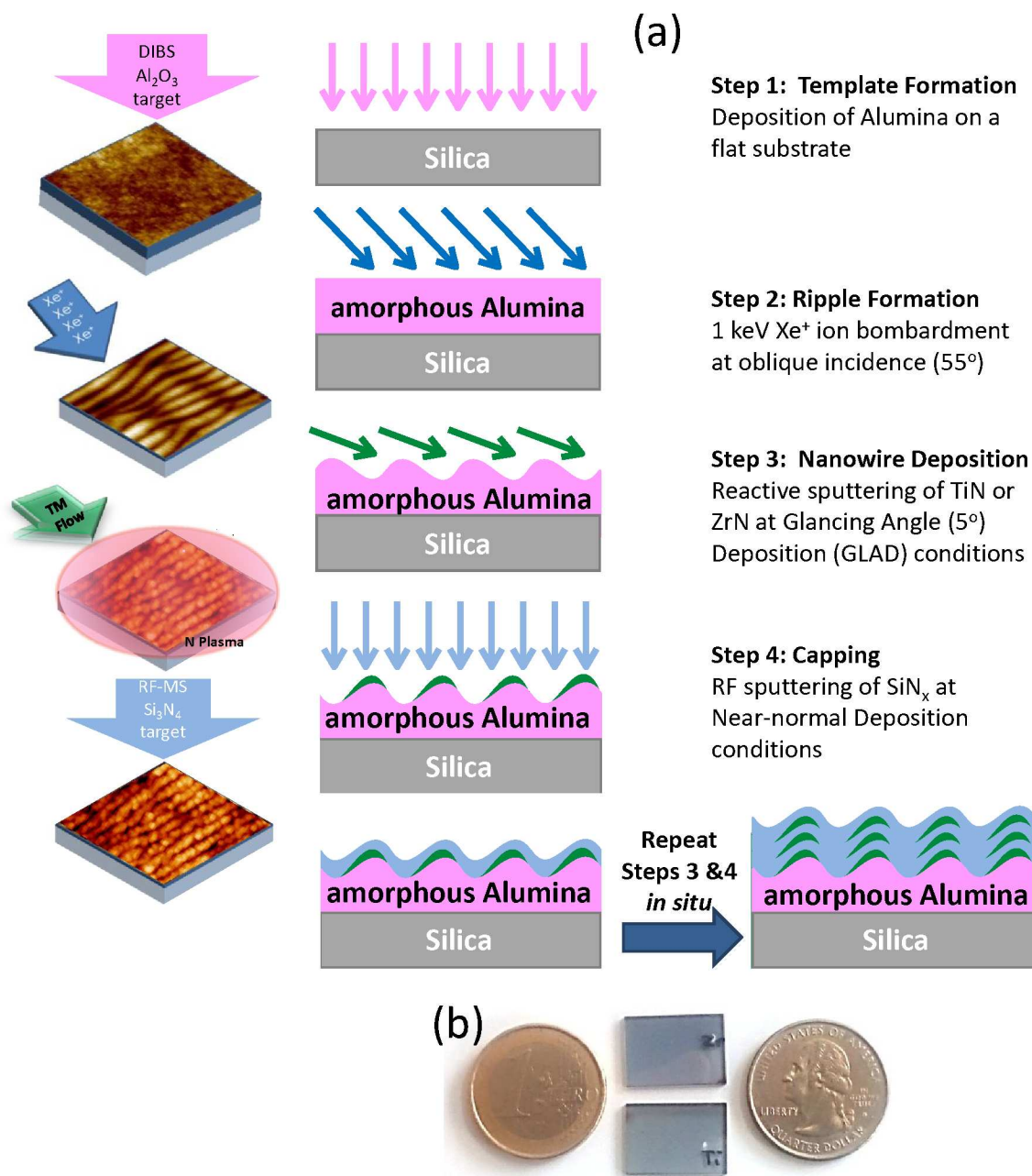
Fig. 1: (a) Schematic of the process used for the bottom-up fabrication of dichroic and plasmonic TMN nanostructures; the left panels are based on AFM images of real samples at each step of the fabrication process. (b) The physical dimensions of the samples compared with a Euro coin and a quarter US dollar; coloration appears only under polarized light.
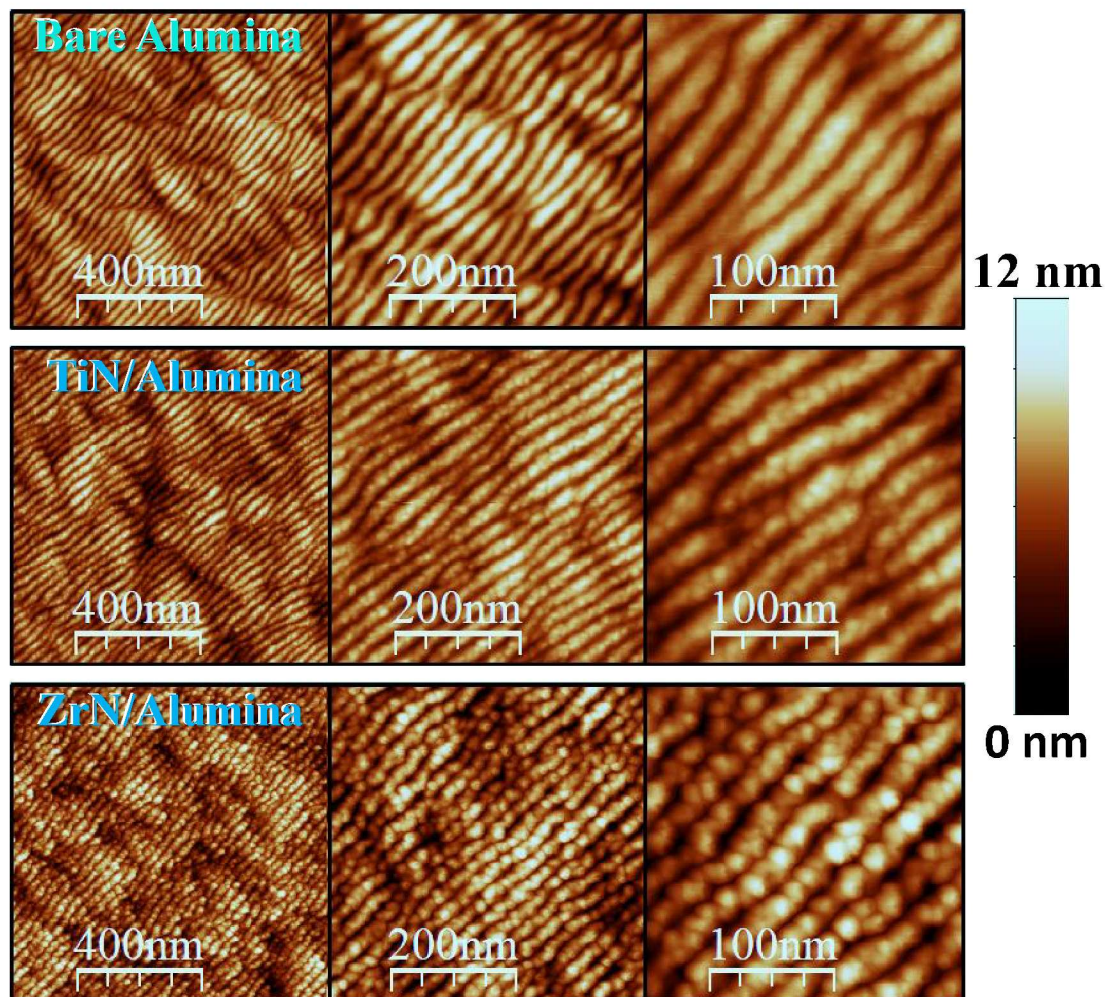
Fig. 2: Morphology of representative NWs of ZrN (lower panels) and TiN (intermediate panels) on rippled alumina substrates (upper panels) as observed by AFM.
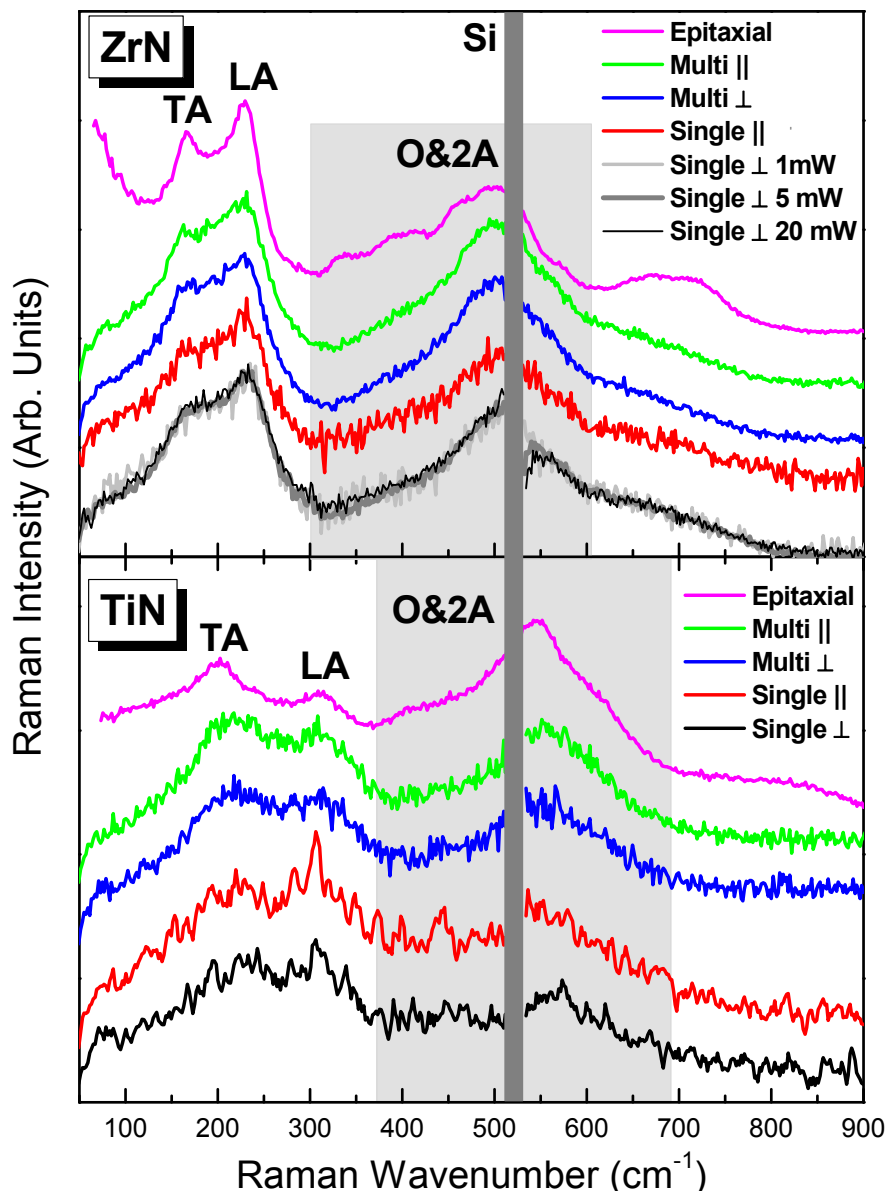
Fig. 3: Polarized Raman spectra of the single- and triple- (multi) arrays of ZrN and TiN nanostructures with the laser beam polarized along (‖) and across (⊥) the ripples; the spectra of the corresponding epitaxial opaque films from Ref. 81 are also shown for comparison. The light grey shaded area indicates the spectral range of the overlapping 2TA, 2LA and O modes (denoted as 2A&O), while the dark grey shaded area indicates the spectral location of the very narrow and strong Raman peak of the Si substrate that is removed from the nitride spectra for clarity.
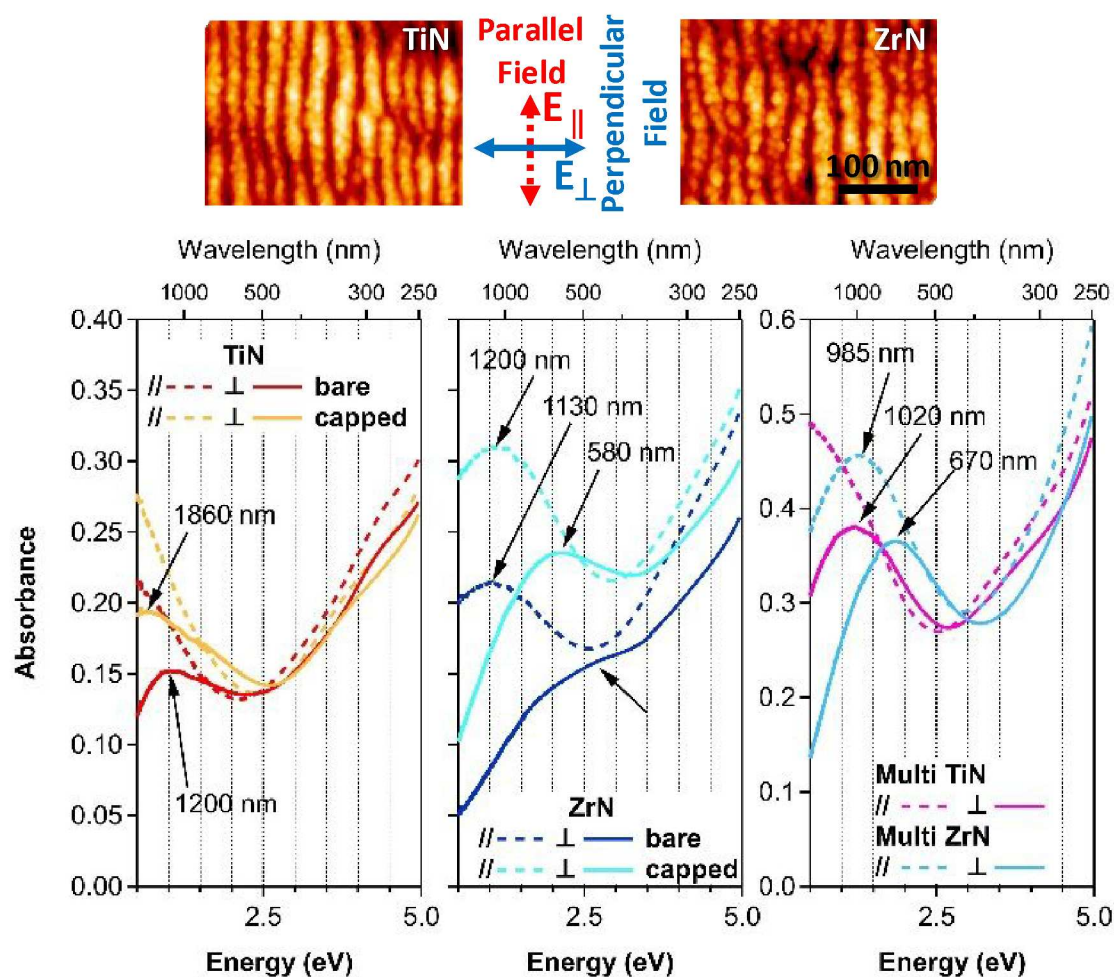
Fig. 4: Optical absorbance spectra of TiN (lower left panel) and ZrN (lower center panel) nanostructures, and multi-stacks (lower right panel), with or without 5 nm SiN$_x$ capping; solid and dotted lines represent data obtained for perpendicular (⊥) and parallel (‖) electric fields, respectively, with respect to the ripples, as defined in the upper panels of the figure. Arrows indicate the spectral positions of the LSPR maximum for each spectrum.
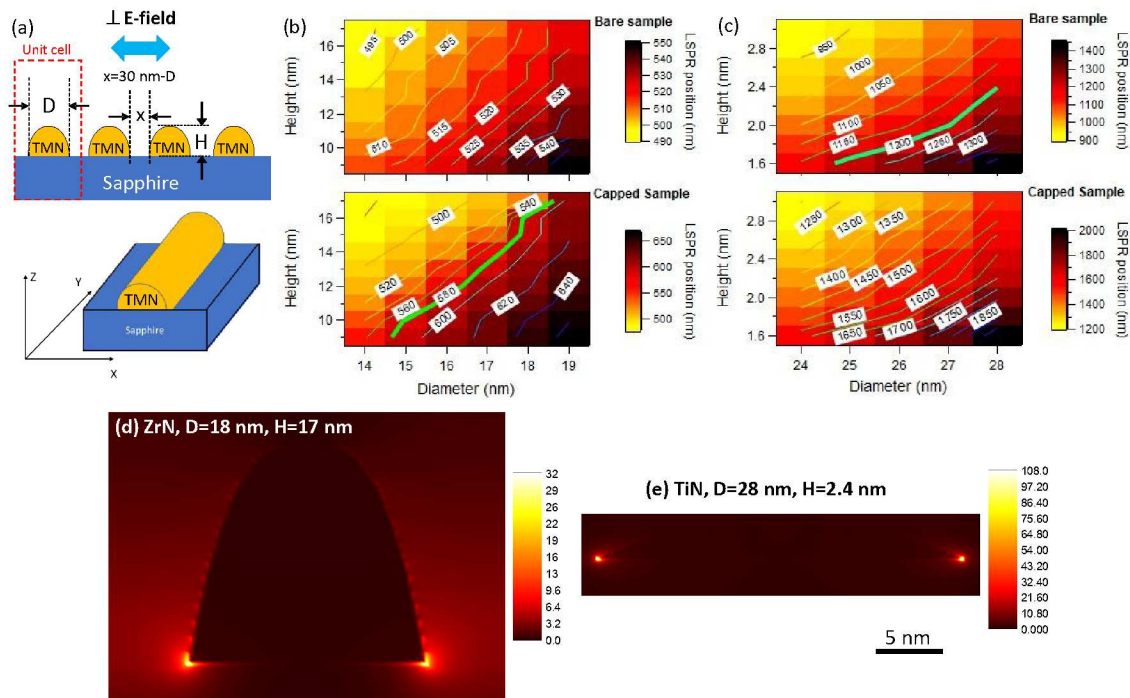
Fig. 5: (a) The geometry of the nanostructures used for the FDTD calculations. (b) Contour plots of the wavelength of maximum absorbance for bare (upper panel) and SiN$_x$-capped (lower panel) ZrN nanostructures for varying diameter (D) and height (H). (c) Contour plots of the wavelength of maximum absorbance for bare (upper panel) and SiN$_x$-capped (lower panel) TiN nanostructures for varying diameter (D) and height (H). The thick green lines correspond to the experimental position. (d,e) Near-field enhancement distributions around bare ZrN and TiN nanostructures for appropriate (*H,D*) values (see text) and laser excitation at 1030 nm.

27
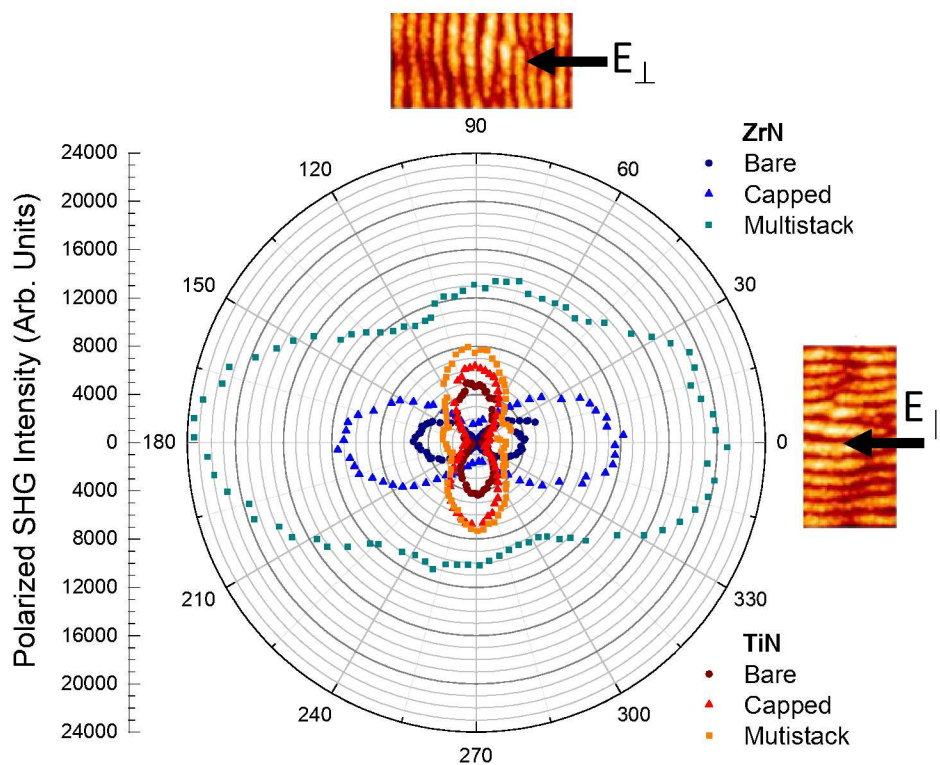
Fig. 6: Polar diagrams of polarized SHG of the ZrN and TiN nanostructures probed by a 1030 nm laser beam; at 0º the electric field polarization is parallel with the ripples of the samples.

ASSOCIATED CONTENT

Supporting Information. The SI section includes:

Figure S1: Linear AFM scans

Figure S2: AFM comparison of single- and multi-layer structures

Figure S3: Optical absorbance spectra calculated by FDTD

Figure S4: The SHG data in cartesian plot

Tables S1, S2: Quantification of Raman analysis

AUTHOR INFORMATION

Corresponding Author

*Panos Patsalas, e-mail: ppats@physics.auth.gr

Author Contributions

The manuscript was written through contributions of all authors. All authors have given

approval to the final version of the manuscript.

ABBREVIATIONS

GLAD, glancing angle deposition; TMN, transition metal nitrides; AFM, atomic force

microscopy; LSPR, localized surface plasmon resonance; FDTD, finite difference time

domain; SHG, second harmonic generation; NIR, near infrared; NW, nanowires.

REFERENCES

1. Patsalas, P.; Logothetidis, S. Interface Properties and Structural Evolution of Nanoscale TiN/Si and TiN/GaN Heterostructures. *Journal of Applied Physics* **2003**, 93, 989-998.

2. Reinholdt, A.; Pecenka, R.; Pinchuk, A.; Runte, S.; Stepanov, A.L.; Weirich, T.E.; Kreibig, U. Structural, compositional, optical and colorimetric characterization of TiN-nanoparticles. *The European Physical Journal D* **2004**, 31, 69-76.

3. Naik G.V.; Kim J.; Boltasseva A. Oxides and nitrides as alternative plasmonic materials in the optical range. *Optical Materials Express* **2011**, 1, 1090-1099.

4. Guler, U.; Boltasseva, A.; Shalaev, V.M. Refractory Plasmonics. *Science* **2014**, 344, 263-264.

5. Patsalas P.; Charitidis C.; Logothetidis S. The effect of substrate temperature and biasing on the mechanical properties and structure of sputtered titanium nitride thin films. *Surface and Coatings Technology* **2000**, 125, 335-340.

6. Abadias G.; Ivashchenko V.I.; Belliard L.; Djemia P. Structure, phase stability and elastic properties in the $Ti_{1-x}Zr_xN$ thin-film system: Experimental and computational studies. *Acta Materialia* **2012**, 60, 5601-5614.

7. Abadias G.; Koutsokeras L.E.; Siozios A.; Patsalas P. Stress, phase stability and oxidation resistance of ternary Ti-Me-N (Me = Zr, Ta) hard coatings. *Thin Solid Films* **2013**, 538, 56-70.

8. Abadias G.; Kanoun M.B.; Goumri-Said S.; Koutsokeras L.; Dub S.N.; Djemia Ph. Electronic structure and mechanical properties of ternary ZrTaN alloys studied by

ab initio calculations and thin-film growth experiments. *Physical Review B* **2014**, 90, art. no. 144107.

9. Gui L.; Bagheri S.; Strohfeldt N.; Hentschel M.; Zgrabik C.M.; Metzger B.; Linnenbank H.; Hu E.L.; Giessen H. Nonlinear Refractory Plasmonics with Titanium Nitride Nanoantennas. *Nano Letters* **2016**, 16, 5708-5713.

10. Sato R.; Ishii S.; Nagao T.; Naito M.; Takeda Y. Broadband Plasmon Resonance Enhanced Third-Order Optical Nonlinearity in Refractory Titanium Nitride Nanostructures. *ACS Photonics* **2018**, 5, 3452-3458.

11. Kinsey N.; Syed A.A.; Courtwright D.; DeVault C.; Bonner C.E.; Gavrilenko V.I.; Shalaev V.M.; Hagan D.J.; Van Stryland E.W.; Boltasseva A. Effective third-order nonlinearities in metallic refractory titanium nitride thin films. *Optical Materials Express* **2015**, 5, 2395-2403.

12. Naik G.V.; Schroeder J.L.; Ni X.; Kildishev A.V.; Sands T.D.; Boltasseva A. Titanium nitride as a plasmonic material for visible and near-infrared wavelengths. *Optical Materials Express* **2012**, 2, 478-489.

13. Naik G.V.; Saha B.; Liu J.; Saber S.M.; Stach E.A.; Irudayaraj J.M.K.; Sands T.D.; Shalaev V.M.; Boltasseva A. Epitaxial superlattices with titanium nitride as a plasmonic component for optical hyperbolic metamaterials. *Proceedings of the National Academy of Sciences of the United States of America* **2014**, 111, 7546-7551.

14. Lu Y.-J.; Sokhoyan R.; Cheng W.-H.; Kafaie Shirmanesh G.; Davoyan A.R.; Pala R.A.; Thyagarajan K.; Atwater H.A. Dynamically controlled Purcell enhancement

of visible spontaneous emission in a gated plasmonic heterostructure. *Nature Communications* **2017**, 8, art. no. 1631.

15. Saha S.; Dutta A.; Kinsey N.; Kildishev A.V.; Shalaev V.M.; Boltasseva A. On-Chip Hybrid Photonic-Plasmonic Waveguides with Ultrathin Titanium Nitride Films. *ACS Photonics* **2018**, 5, 4423-4431.

16. Chaudhuri K.; Shaltout A.; Shah D.; Guler U.; Dutta A.; Shalaev V.M.; Boltasseva A. Photonic Spin Hall Effect in Robust Phase Gradient Metasurfaces Utilizing Transition Metal Nitrides. *ACS Photonics* **2019**, 6, 99-106.

17. Habib A.; Florio F.; Sundararaman R. Hot carrier dynamics in plasmonic transition metal nitrides. *Journal of Optics UK* **2018**, 20, art. no. 064001.

18. Metaxa C.; Kassavetis S.; Pierson J.F.; Gall D.; Patsalas P. Infrared Plasmonics with Conductive Ternary Nitrides. *ACS Applied Materials and Interfaces* **2017**, 9, 10825-10834.

19. Lalisse A.; Tessier G.; Plain J.; Baffou G. Plasmonic efficiencies of nanoparticles made of metal nitrides (TiN, ZrN) compared with gold. *Scientific Reports* **2016**, 6, art. no. 38647.

20. Kassavetis S.; Bellas D.V.; Abadias G.; Lidorikis E.; Patsalas P. Plasmonic spectral tunability of conductive ternary nitrides. *Applied Physics Letters* **2016**, 108, art. no. 263110.

21. Patsalas P.; Kalfagiannis N.; Kassavetis S.; Abadias G.; Bellas D.V.; Lekka C.; Lidorikis E. Conductive nitrides: Growth principles, optical and electronic properties, and their perspectives in photonics and plasmonics. *Materials Science and Engineering R: Reports* **2018**, 123, 1-55.

32

22.   Naik G.V.; Shalaev V.M.; Boltasseva A. Alternative plasmonic materials: Beyond

        gold and silver. *Advanced Materials* **2013**, 25, 3264-3294.

23.   Li W.; Guler U.; Kinsey N.; Naik G.V.; Boltasseva A.; Guan J.; Shalaev V.M.;

        Kildishev A.V. Refractory plasmonics with titanium nitride: Broadband. *Advanced*

        Materials **2014**, 26, 7959-7965.

24.   Briggs J.A.; Naik G.V.; Zhao Y.; Petach T.A.; Sahasrabuddhe K.; Goldhaber-

        Gordon D.; Melosh N.A.; Dionne J.A. Temperature-dependent optical properties of

        titanium nitride. *Applied Physics Letters* **2017**, 110, art. no. 101901.

25.   West P.R.; Ishii S.; Naik G.V.; Emani N.K.; Shalaev V.M.; Boltasseva A.

        Searching for better plasmonic materials. *Laser and Photonics Reviews* **2010**, 4,

        795-808.

26.   Blaber M.G.; Arnold M.D.; Ford M.J. A review of the optical properties of alloys

        and intermetallics for plasmonics. *Journal of Physics Condensed Matter* **2010**, 22,

        art. no. 143201.

27.   Guler U.; Shalaev V.M.; Boltasseva A. Nanoparticle plasmonics: Going practical

        with transition metal nitrides. *Materials Today* **2015**, 18, 227-237.

28.   Karaballi, R.A.; Esfahani Monfared, Y.; Dasog, M. Photothermal Transduction

        Efficiencies of Plasmonic Group 4 Metal Nitride Nanocrystals. *Langmuir* **2020**, 36,

        5058–5064.

29.   Karaballi, R.A.; Humagain, G.; Fleischman, B.R.A.; Dasog, M. Synthesis of

        Plasmonic Group-4 Nitride Nanocrystals by Solid-State Metathesis. *Angewandte*

        Chemie International Edition **2019**, 58, 3147-3150.

30. Rodriguez, C.B.; Barragan, A.A.; Nava, G.; Exarhos, S.; Mangolini, L. Stabilizing the Plasmonic Response of Titanium Nitride Nanocrystals with a Silicon Oxynitride Shell: Implications for Refractory Optical Materials. *ACS Applied Nano Materials* **2020**, 3, 4504–4511.

31. Barragan, A.A.; Ilawe, N.V.; Zhong, L.; Wong, B.M.; Mangolini, L. A Non-Thermal Plasma Route to Plasmonic TiN Nanoparticles. *J. Physical Chemistry C* **2017**, 121, 4, 2316–2322

32. Matenoglou G.M.; Koutsokeras L.E.; Lekka Ch.E.; Abadias G.; Kosmidis C.; Evangelakis G.A.; Patsalas P. Structure, stability and bonding of ternary transition metal nitrides. *Surface and Coatings Technology* **2009**, 204, 911-914.

33. Shah D.; Reddy H.; Kinsey N.; Shalaev V.M.; Boltasseva A. Optical Properties of Plasmonic Ultrathin TiN Films. *Advanced Optical Materials* **2017**, 5, art. no. 1700065.

34. Hu; J; Ren; X.; Reed; A.N.; Reese; T.; Rhee; D.; Howe; B.; Lauhon; L.J.; Urbas; A.; Odom; T.W. Evolutionary Design and Prototyping of Single Crystalline Titanium Nitride Lattice Optics. *ACS Photonics* **2017**, 4, 606-612.

35. Briggs J.A.; Naik G.V.; Petach T.A.; Baum B.K.; Goldhaber-Gordon D.; Dionne J.A. Fully CMOS-compatible titanium nitride nanoantennas. *Applied Physics Letters* **2016**, 108, art. no. 51110.

36. Murai S.; Fujita K.; Daido Y.; Yasuhara R.; Kamakura R.; Tanaka K. Plasmonic arrays of titanium nitride nanoparticles fabricated from epitaxial thin films. *Optics Express* **2016**, 24, 1143-1153.

37. Guler U.; Ndukaife J.C.; Naik G.V.; Nnanna A.G.A.; Kildishev A.V.; Shalaev V.M.; Boltasseva A. Local heating with lithographically fabricated plasmonic titanium nitride nanoparticles. *Nano Letters* **2013**, 13, 6078-6083.

38. Dutta A.; Kinsey N.; Saha S.; Guler U.; Shalaev V.M.; Boltasseva, A. Plasmonic interconnects using zirconium nitride, Conference on Lasers and Electro-Optics. *Optical Society of America Technical Digest* **2016**, art. no. JW2A.86.

39. Kamakura R.; Murai S.; Fujita K.; Tanaka K. Enhanced Photoluminescence from Organic Dyes Coupled to Periodic Array of Zirconium Nitride Nanoparticles. *ACS Photonics* **2018**, 5, 3057-3063.

40. Howell I.R.; Giroire B.; Garcia A.; Li S.; Aymonier C.; Watkins J.J. Fabrication of plasmonic TiN nanostructures by nitridation of nanoimprinted TiO_2 nanoparticles. *Journal of Materials Chemistry C* **2018**, 6, 1399-1406.

41. Bagheri S.; Zgrabik C.M.; Gissibl T.; Tittl A.; Sterl F.; Walter R.; De Zuani S.; Berrier A.; Stauden T.; Richter G.; Hu E.L.; Giessen H. Large-area fabrication of TiN nanoantenna arrays for refractory plasmonics in the midinfrared by femtosecond direct laser writing and interference lithography. *Optical Materials Express* **2015**, 5, 2625-2633.

42. Balasubramanian K.; Khare S.V.; Gall D. Energetics of point defects in rocksalt structure transition metal nitrides: Thermodynamic reasons for deviations from stoichiometry. *Acta Materialia* **2018**, 159, 77-88.

43. Tsetseris L.; Kalfagiannis N.; Logothetidis S.; Pantelides S.T. Trapping and release of impurities in TiN: A first-principles study. *Physical Review B* **2008**, 78, art. no. 094111.

44. Spengler; W.; Kaiser; R.; Christensen; A.N.; Mueller-Vogt; G. Raman scattering, superconductivity, and phonon density of states of stoichiometric and nonstoichiometric TiN. *Physical Review B* **1978,** 17, 1095-1101.

45. Patsalas P. Zirconium nitride: A viable candidate for photonics and plasmonics?. *Thin Solid Films* **2019**, 688, art. no. 137438.

46. Chen T.-Y.; Obermeier J.; Schumacher T.; Lin F.-C.; Huang J.-S.; Lippitz M.; Huang C.-B. Modal Symmetry Controlled Second-Harmonic Generation by Propagating Plasmons. *Nano Letters* **2019**, 19, 6424−6428.

47. Psilodimitrakopoulos S.; Mouchliadis L. Paradisanos I.; Lemonis A.; Kioseoglou G.; Stratakis E. Ultrahigh-resolution nonlinear optical imaging of the armchair orientation in 2D transition metaldichalcogenides. *Light: Science and Applications* **2018**, 7, art. no. 18005.

48. Camelio S.; Babonneau D.; Lantiat D.; Simonot L.; Pailloux F. Anisotropic optical properties of silver nanoparticle arrays on rippled dielectric surfaces produced by low-energy ion erosion. *Physical Review B* **2009**, 80, art. no. 155434.

49. Babonneau D.; Camelio S.; Simonot L.; Pailloux F.; Guérin P.; Lamongie B.; Lyon O. Tunable plasmonic dichroism of Au nanoparticles self-aligned on rippled Al_2O_3 thin films. *Euro Physics Letters 2011*, 93, art. no. 26005.

50. Babonneau D.; Vandenhecke E.; Camelio S. Formation of nanoripples on amorphous alumina thin films during low-energy ion-beam sputtering: experiments and simulations. *Physical Review B* **2017**, 95, art. no. 085412.

51. Kaxiras, E. Atomic and Electronic Structure of Solids. p. 198, Cambridge University Press, Cambridge (2003).

52. Koutsokeras L.E.; Matenoglou G.M.; Patsalas P. Structure, electronic properties and electron energy loss spectra of transition metal nitride films. *Thin Solid Films* **2013**, 528, 49-52.

53. Matenoglou G.M.; Koutsokeras L.E.; Patsalas P. Plasma energy and work function of conducting transition metal nitrides for electronic applications. *Applied Physics Letters* **2009**, 94, art. no. 152108.

54. Anders A. A structure zone diagram including plasma-based deposition and ion etching. *Thin Solid Films* **2010**, 518, 4087-4090.

55. Patsalas P.; Gravalidis C.; Logothetidis S. Surface kinetics and subplantation phenomena affecting the texture, morphology, stress, and growth evolution of titanium nitride films. *Journal of Applied Physics* **2004**, 96, 6234-6246.

56. Uglov V.V.; Abadias G.; Zlotski S.V.; Saladukhin I.A.; Safronov I.V.; Shymanski V.I.; Janse van Vuuren A.; O'Connell J.; Skuratov V.; Neethling J.H., Features of microstructure of ZrN, Si_3N_4 and ZrN/SiN_x nanoscale films irradiated by Xe ions. *Vacuum* **2017**, 143, 491-494.

57. Abadias G.; Koutsokeras L.E.; Guerin Ph.; Patsalas P. Stress Evolution in Magnetron Sputtered Ti–Zr–N and Ti–Ta–N Films Studied by In-Situ Wafer Curvature: Role of Energetic Particles. *Thin Solid Films* **2009**, 518, 1532–1537.

58. Mareus, R.; Mastail, C.; Anğaya, F.; Brunetière, N.; Abadias, A. Study of columnar growth, texture development and wettability of reactively sputter-deposited TiN, ZrN and HfN thin films at glancing angle incidence. *Surface and Coatings Technology* **2020**, 399, 15, art. no. 126130

59. Kassavetis S.; Ozsdolay B.D.; Kalfagiannis N.; Habib A.; Tortai J.-H.; Kerdsongpanya S.; Sundararaman R.; Stchakovsky M.; Bellas D.V.; Gall D.; Patsalas P. Near-zero negative real permittivity in far ultraviolet: Extending plasmonics and photonics with B1-MoN$_x$. *J. Phys. Chem. C* **2019**, 123, 21120-21129.

60. Abadias, G.; Lib, C.-H.; Belliard, L.; Hu, Q.M.; Greneche, N.; Djemia, P. Large influence of vacancies on the elastic constants of cubic epitaxial tantalum nitride layers grown by reactive magnetron sputtering. *Acta Materialia* **2020**, 184, 254-266.

61. Karl P.; Ubl M.; Hentschel M.; Flad P.; Chiao Z.-Y.; Yang J.-W.; Lu Y.-J.; Giessen H. Optical properties of niobium nitride plasmonic nanoantennas for the near- and mid-infrared spectral range. *Optical Materials Express* **2020**, 10, 2597-2606.

62. Hillier J. A.; Camelio S.; Cranton W.; Nabok A. V.; Mellor C. J.; Koutsogeorgis D.C.; Kalfagiannis N. When Ellipsometry Works Best - A Case Study with Transparent Conductive Oxides. *ACS Photonics* **2020**, 7, 2692–2702.

63. Kapetanovic V.; Bicket I.C.; Lazar S.; Lagos M.J.; Botton G.A. Tunable Infrared Plasmon Response of Lithographic Sn-doped Indium Oxide Nanostructures, *Advanced Optical Materials* **2020**, 8, art. no. 2001024.

64. Sarma B.K.; Rajkumar P. Al-doped ZnO transparent conducting oxide with appealing electro-optical properties – Realization of indium free transparent conductors from sputtering targets with varying dopant concentrations. *Materials Today Communications* **2020**, 23, art. no. 100870.

65. Zhu C.; Li J.; Yang Y.; Huang J.; Lu Y.; Tan R.; Dai N.; Song W. Zn-aided defect control for ultrathin GZO films with high carrier concentration aiming at alternative plasmonic metamaterials. *Physica Status Solidi A* **2015**, 212, 1713-1718.

66. Ngo H.D.; Chen K.; Handegård O.S.; Doan A.T.; Ngo T.D.; Dao T.D.; Ikeda N.; Ohi A.; Nabatame T.; Nagao T. Nanoantenna structure with mid-infrared plasmonic niobium-doped titanium oxide. *Micromachines* **2020**, 11, 1-23.

67. Liu Y.; Zhang H.; Ouyang P.; Chen W.; Wang Y.; Li Z. High electrochemical performance and phase evolution of magnetron sputtered MoO_2 thin films with hierarchical structure for Li-ion battery electrodes. *Journal of Materials Chemistry A* **2014**, 2, 4714-4721.

68. Fernandes Cauduro A.L.; Fabrim Z.E.; Ahmadpour M.; Fichtner P.F.P.; Hassing Sø.; Rubahn H.-G.; Madsen M. Tuning the optoelectronic properties of amorphous MoO_x films by reactive sputtering. *Applied Physics Letters* **2015**, 106, art. no 202101.

69. Collado V.; Martin N.; Pedrosa P.; Rauch J.-Y.; Horakova M.; Yazdi M.A.P.; Billard A. Temperature dependence of electrical resistivity in oxidized vanadium films grown by the GLAD technique. *Surface and Coatings Technology* **2016**, 304, 476-485.

70. Okimura K.; Kubo N. Preparation of VO_2 films with metal-insulator transition on sapphire and silicon substrates by inductively coupled plasma-assisted sputtering. *Japanese Journal of Applied Physics Letters* **2005**, 44, L1150-L1153.

71. Cortie M.B.; Arnold M.D.; Keast V.J. The Quest for Zero Loss: Unconventional Materials for Plasmonics. *Advanced Materials* **2020**, 32, art. no. 1904532.

72. Gutiérrez Y.; Brown A.S.; Moreno F.; Losurdo M. Plasmonics beyond noble

metals: Exploiting phase and compositional changes for manipulating plasmonic

performance. *J. Appl. Phys.* **2020**, 128, art. no. 080901.

73. Zhang Q.; Li X.; Ma Q.; Zhang Q.; Bai H.; Yi W.; Liu J.; Han J.; Xi G. A metallic

molybdenum dioxide with high stability for surface enhanced Raman spectroscopy.

Nature Communications **2017**, 8, art. no. 14903.

74. Etman A.S.; Wang L.; Edström K.; Nyholm L.; Sun J. Molybdenum Oxide

Nanosheets with Tunable Plasmonic Resonance: Aqueous Exfoliation Synthesis

and Charge Storage Applications. *Advanced Functional Materials* **2019**, 29, art. no.

1806699.

75. Zhan Y.; Liu Y.; Zu H.; Guo Y.; Wu S.; Yang H.; Liu Z.; Lei B.; Zhuang J.; Zhang

X.; Huang D.; Hu C. Phase-controlled synthesis of molybdenum oxide

nanoparticles for surface enhanced Raman scattering and photothermal therapy.

Nanoscale **2018**, 10, 5997-6004.

76. Kalantari Osgouei A.; Hajian H.; Khalichi B.; Serebryannikov A.E.; Ghobadi A.;

Ozbay E. Active Tuning from Narrowband to Broadband Absorbers Using a Sub-

wavelength VO_2 Embedded Layer. *Plasmonics* **2021**, in press.

77. Duan X.; White S.T.; Cui Y.; Neubrech F.; Gao Y.; Haglund R.F.; Liu N.

Reconfigurable Multistate Optical Systems Enabled by VO_2 Phase Transitions.

ACS Photonics **2020**, 7, 2958-2965.

78. Schrecongost D.; Xiang Y.; Chen J.; Ying C.; Zhang H.-T.; Yang M.; Gajurel P.;

Dai W.; Engel-Herbert R.; Cen C. Rewritable Nanoplasmonics through Room-

40

Temperature Phase Manipulations of Vanadium Dioxide. *Nano Letters* **2020**, 20, 7760-7766.

79.   Butakov N.A.; Valmianski I.; Lewi T.; Urban C.; Ren Z.; Mikhailovsky A.A.; Wilson S.D.; Schuller I.K.; Schuller J.A. Switchable Plasmonic-Dielectric Resonators with Metal-Insulator Transitions, *ACS Photonics* **2018**, 5, 371-377.

80.   Christensen A.N.; Dietrich O.W.; Kress W.; Teuchert W.D. Phonon anomalies in transition-metal nitrides: ZrN. *Physical Review B* **1979**, 19, 5699-5703.

81.   Gioti M.; Arvanitidis J.; Christofilos D.; Chaudhuri K.; Zorba T.; Abadias G.; Gall D.; Shalaev V.M.; Boltasseva A.; Patsalas P. Plasmonic and phononic properties of epitaxial conductive transition metal nitrides. *Journal of Optics UK* **2020**, 22, art. no. 084001.

82.   Spengler W.; Kaiser R. First and second order Raman scattering in transition metal compounds. *Solid State Communications* **1976**, 18, 881-884.

83.   Stoehr M.; Shin C.-S.; Petrov I.; Greene J.E. Raman scattering from TiN_x (0.67≤x≤1.00) single crystals grown on MgO(001). *Journal of Applied Physics* **2011**, 110, art. no. 083503.

84.   Abdallah B.; Naddaf M.; A-Kharroub M. Structural, mechanical, electrical and wetting properties of ZrN_x films deposited by Ar/N_2 vacuum arc discharge: Effect of nitrogen partial pressure. *Nuclear Instruments and Methods in Physics Research B* **2013**, 298, 55-60.

85.   Balliu E.; Andersson H.; Engholm M.; Öhlund T.; Nilsson H.-E.; Olin H. Selective laser sintering of inkjet-printed silver nanoparticle inks on paper substrates to achieve highly conductive patterns. *Scientific Reports* **2018**, 8, art. no. 10408.

41

86. Kalfagiannis N.; Siozios A.; Bellas D.V.; Toliopoulos D.; Bowen L.; Pliatsikas N.; Cranton W.M.; Kosmidis C.; Koutsogeorgis D.C.; Lidorikis E.; Patsalas P. Selective modification of nanoparticle arrays by laser-induced self-assembly (MONA-LISA): putting control into bottom-up plasmonic nanostructuring. *Nanoscale* **2016**, 8, 8236-44.

87. Siozios A.; Kalfagiannis N.; Bellas D.V.; Bazioti C.; Dimitrakopulos G.P.; Vourlias G.; Cranton W.M.; Lidorikis E.; Koutsogeorgis D.C.; Patsalas, P. Sub-surface laser nanostructuring in stratified metal/dielectric media: a versatile platform towards flexible, durable and large scale plasmonic writing. *Nanotechnology* **2015**, 26, art. no. 155301.

88. Patsalas P.; Kalfagiannis N.; Kassavetis S. Optical properties and plasmonic performance of titanium nitride. *Materials* **2015**, 8, 3128-3154.

89. Shah D.; Catellani A.; Reddy H.; Kinsey N.; Shalaev V.M.; Boltasseva A.; Calzolari A. Controlling the plasmonic properties of ultrathin TiN films at the atomic level. *ACS Photonics* **2018**, 5, 2816–2824.

90. Hentschel M.; Dregely D.; Vogelgesang R.; Giessen H.; Liu N. Plasmonic oligomers: The role of individual particles in collective behavior. *ACS Nano* **2011**, 5, 2042-2050.

91. Sweatlock L.A.; Maier S.A.; Atwater H.A.; Penninkhof J.J.; Polman A. Highly confined electromagnetic fields in arrays of strongly coupled Ag nanoparticles. *Physical Review B* **2005**, 71, art. no 235408.

92.   Camelio, S.; Vandenhecke, E.; Rousselet, S.; Babonneau, D. Optimization of

       growth and ordering of Ag nanoparticle arrays on ripple patterned alumina surfaces

       for strong plasmonic coupling. *Nanotechnology* **2014**, 25, art. no. 035706.

93.   Lidorikis, E.; Egusa, S; Joannopoulos, J.D. Effective medium properties and

       photonic crystal superstructures of metallic nanoparticle arrays. *J. Appl. Phys.*

       2007, 101, art. no. 54304.

94.   Schedin F.; Lidorikis L.; Lombardo A.; Kravets V.G.; Geim A.K.; Grigorenko

       A.N.; Novoselov K.S.; Ferrari A.C. Surface-enhanced Raman spectroscopy of

       graphene. *ACS Nano* **2010**, 4, 5617–5626.

95.   Herzog J.B.; Knight M.W.; Li Y.; Evans K.M.; Halas N.J.; Natelson D. Dark

       plasmons in hot spot generation and polarization in interelectrode nanoscale

       junctions, *Nano Letters* **2013**, 13, 1359-1364.

96.   Matranga C.; Guyot-Sionnest P. Absolute intensity measurements of the optical

       second-harmonic response of metals from 0.9 to 2.5 eV. *J. Chem. Phys.* **2001**, 115,

       9503-9512.

97.   Kujala S.; Canfield B.K.; Kauranen M.; Svirko Y.; Turunen J. Multipole

       interference in the second-harmonic optical radiation from gold nanoparticles.

       Physical Review Letters **2007**, 98, art. no. 167403.

98.   Chen T.-Y.; Obermeier J.; Schumacher T.; Lin F.-C.; Huang J.-S.; Lippitz M.;

       Huang C.-B. Modal Symmetry Controlled Second-Harmonic Generation by

       Propagating Plasmons. *Nano Letters* **2019**, 19, 6424−6428.

99.   Capretti A.; Wang Y.; Engheta N.; Dal Negro L. Comparative Study of Second-

       Harmonic Generation from Epsilon-Near-Zero Indium Tin Oxide and Titanium

Nitride Nanolayers Excited in the Near-Infrared Spectral Range. *ACS Photonics* **2015**, 2, 1584-1591.

100. O'Brien K.; Suchowski H.; Rho J.; Salandrino A.; Kante B.; Yin X.; Zhang X. Predicting nonlinear properties of metamaterials from the linear response. *Nature Materials* **2015**, 14, 379–383.

101. Husu H.; Siikanen R.; Mäkitalo J.; Lehtolahti J.; Laukkanen J.; Kuittinen M.; Kauranen M. Metamaterials with Tailored Nonlinear Optical Response. *Nano Letters* **2012**, 12, 673−677.

102. Galanty M.; Shavit O.; Weissman A.; Aharon H.; Gachet D.; Segal E.; Salomon A. Second harmonic generation hotspot on a centrosymmetric smooth silver surface. *Light: Science and Appl.* **2018**, 7, art. no. 49.

103. Wen X.; Li G.; Gu C.; Zhao J.; Wang S.; Jiang C.; Palomba S.; Martijn De Sterke C.; Xiong Q. Doubly Enhanced Second Harmonic Generation through Structural and Epsilon-near-Zero Resonances in TiN Nanostructures. *ACS Photonics* **2018**, 5, 2087-2093.

104. Venkataramanababu S.; Nair G.; Deshpande P.; Jithin M.A.; Mohan S.; Ghosh A. Chiro-plasmonic refractory metamaterial with titanium nitride (TiN) core-shell nanohelices. *Nanotechnology* **2018**, 29, art. no. 255203.

105. Huang J.; Wang X.; Hogan N.L.; Wu S.; Lu P.; Fan Z.; Dai Y.; Zeng B.; Starko-Bowes R.; Jian J.; Wang H.; Li L.; Prasankumar R.P.; Yarotski D.; Sheldon M.; Chen H.-T.; Jacob Z.; Zhang X.; Wang H. Nanoscale Artificial Plasmonic Lattice in Self-Assembled Vertically Aligned Nitride–Metal Hybrid Metamaterials. *Advanced Science* **2018**, 5, art. no. 1800416.

44

106. Sharma D.K.; Chaubey S.K.; Vasista A.B.; Karumancheril J.J.; Tripathi R.P.N.; Bouhelier A.; Pavan Kumar G.V. Directional second-harmonic generation controlled by sub-wavelength facets of an organic mesowire. *Applied Optics* **2018**, 57, 5914-5922.